Relict landscapes and fluvial landforms: Catastrophic outflow following a major Late Messinian base-level fall

Dia Ninkabou[a,b], Julien Gargani[c], Christian Gorini[a], Jean-Loup Rubino[b], Roger Urgeles[d], Romain Pellen[e], Damien Do Couto[a], Alexandre Lethiers[a], Bilal Haq[a,f] , and Jimmy Moneron[a,*]

(corresponding author: jimmy.moneron@sorbonne-universite.fr)

[a] *ISTeP, Sorbonne Université, CNRS, 75005 Paris, France*

[b] *Total E&P, 92078 La Défense, France*

[c] *GEOPS, Univ. Paris-Saclay, CNRS, 91405 Orsay, France*

[d] *Institut de Ciències del Mar (CSIC), 08003 Barcelona, Spain*

[e] *LGO, Univ. de Bretagne Occidentale, CNRS, 29280 Plouzané, France*

[f] *George Mason University, Fairfax, Virginia, USA*

Abstract

During the Messinian Salinity Crisis (MSC), the entire Mediterranean Basins underwent dramatic canyon incision along its margins due to fluctuating sea levels and rapidly increasing salinity. However, the specific processes and water sources responsible for such profound landscape transformations have yet to be quantitatively demonstrated. In this study, we combine high resolution 3D seismic reflection data with paleo-stream network geomorphic analyses to reveal two distinct phases of fluvial activity within the Messinian Ebro Valley. The first phase is marked by an exceptional discharge of 240,000 m^3/s, which rapidly carved a 700-meter-deep valley. This intense incision was followed by a period of more moderate flow, during which the newly-formed valley developed alluvial terraces. Our

findings suggest that regressive erosion during the MSC lowstand breached the previously endorheic Ebro Basin, triggering a catastrophic outburst flood and the formation of an extensive drainage network. This event marks the transition from a broad, erosive system to a more confined, meandering river. By refining the timing of this outflow event to the MSC, our study challenges earlier models that positioned the Ebro Basin's opening at an earlier time. This most likely represents the first documented case of an endorheic basin complete drainage due to MSC-induced regressive erosion, providing new insights into the dynamics of this major geological period. **Keywords: Messinian Salinity Crisis, Catastrophic outburst flood, Endorheic basin drainage, Seismic reflection data, Fluvial incision**

Highlights

- 3D seismic reflection data analyses reveal relict Messinian Ebro drainage patterns
- Discharge estimates show an initial outburst flood (~2.4×10^5 m^3/s)
- Lowstand-induced regressive erosion breached the Ebro endorheic basin
- Post-outburst meandering channels cut terraces, recording rapid MSC incision
- Results place Ebro Basin opening in the MSC, challenging pre-MSC capture models

1. Introduction

Abrupt transitions in fluvial dynamics, including catastrophic flooding, are rare but represent some of the most dramatic episodes of landscape evolution on Earth (Gupta et al., 2007) and Mars (Warner et al., 2010). Such events can profoundly reorganise drainage systems at continental scales and are commonly linked to climatic or sea-level change (Baker and Milton, 1974), multi-causal erosional processes (Loget et al., 2005), or, more rarely, volcanic activity (Leverington, 2011). One of the most extreme natural contexts in which large-scale fluvial incision occurred is the Messinian Salinity Crisis (MSC; 5.97–5.33 Ma; Krijgsman et al., 1999), during which major base-level variations induced widespread regressive erosion along Mediterranean margins (Chumakov, 1973; Ryan, 1976; Clauzon, 1982). The MSC, known for massive evaporite accumulation in deep and peripheral basins (Haq et al., 2020), is associated with the development of the Messinian Erosional Surface (MES; Fig. 1), a regionally extensive unconformity documented throughout the Mediterranean Sea (Guennoc et al., 2000; Lofi et al., 2005, 2011; Heida et al., 2022; Moneron et al., 2024).

Advances in seismic reflection imaging have substantially improved the identification and mapping of Messinian drainage systems, enabling more detailed investigation of the MES and associated canyon networks in the western (e.g., Urgeles et al., 2011) and eastern (Moneron et al., 2024) Mediterranean Sea basins. Messinian canyons have also been documented along numerous Mediterranean margins, including the Nile Delta (Barber, 1981), the Rhône system (Clauzon, 1982; Gargani, 2004), the Ebro Margin (Urgeles et al., 2011), and the Levant

margin (Druckman et al., 1995). Despite extensive documentation of these features (Gargani and Rigollet, 2007; Moneron et al., 2025), the hydrological conditions and process-based mechanisms capable of generating such deep and rapid incision remain relatively poorly constrained.

The MSC itself has long been characterised by intense debate regarding the magnitude, timing, and spatial extent of Mediterranean base-level drawdown, particularly whether canyon incision occurred under conditions predominantly subaerial (maximum drawdown estimated to be between 1.5 to 2 km, Clauzon, 1982, Loget et al., 2005, Bache et al., 2009; Aloisi et al., 2025) or mostly submarine (Roveri et al., 2014b; Gvirtzman et al., 2022) with hundreds of studies covering the debate (e.g., Madof et al., 2019; Moneron and Gvirtzman, 2022; reviewed by Roveri et al., 2025). Although the existence of a Messinian fluvial pathway in the Ebro region was previously debated (Evans and Arche, 2002; García-Castellanos et al., 2003; Babault et al., 2006), the publication of high-resolution 3D seismic data (covering ~2700 km² of the Ebro region) demonstrated the presence of a deeply incised Messinian valley and partly resolved the question of a fluvial setting along this margin (Urgeles et al., 2011, Pellen et al., 2019). Urgeles et al. (2011) documented a ~700 m-deep valley incised into the MES, characterised by a dendritic drainage network, and used backstripping and isostatic modeling to argue for a major Messinian sea-level drawdown and early opening of the Ebro Basin. Supported by borehole calibration and onshore geological constraints, that study established a robust stratigraphic and tectonic framework for Messinian incision (Urgeles et al., 2011). Importantly, it must also be noted that while the MES

provides a robust stratigraphic marker for major incision along Mediterranean margins, the absolute timing of excavation of the Ebro valley within the MSC relies on the seismic–stratigraphic framework, borehole calibration, and regional Messinian correlations developed by Urgeles et al. (2011), Cameselle et al. (2014) and references therein, rather than on new direct chronological constraints.

Building on this foundation, we revisit the morphology of the MES with different objective and methodological emphasis: rather than constraining the magnitude of base-level fall or the timing of basin opening, we treat the MES as a paleo-topographic surface and apply quantitative geomorphic analyses commonly used for modern river systems to reconstruct the evolution of the paleo-Ebro River.

Our results reveal multi-phase fluvial erosion and raise the question of how a comparatively small drainage basin such as that associated with the paleo-Ebro (~100,000 km²; Fig. 1) could have generated such rapid and deep incision. We interpret these observations to indicate that the formerly endorheic Ebro Basin was breached and largely drained during the MSC, contrasting with earlier models that proposed an earlier (13–8.5 Ma) opening of the basin through fluvial capture and sediment overfilling, in which breaching was inferred to predate the MSC based on Miocene drainage patterns and onshore geological constraints (García-Castellanos et al., 2003; Urgeles et al., 2011; Pellen et al., 2019).

In what follows, we document the morphology and chronological development of the Messinian Ebro Canyon, quantify its hydrogeological evolution, and assess its role within the broader context of the MSC.

2. Background

2.1 Geological setting

The Ebro Margin is a passive continental margin forming the western branch of the Valencia Trough, located between the Iberian Peninsula and the Balearic Promontory (Fig. 1). It developed as an aborted back-arc rift during Oligocene–Early Miocene extension related to rollback of the Apennines–Maghrebide subduction system (Olivet, 1996; Gueguen et al., 1998). Extension reactivated inherited Paleogene structures of the Catalan Coastal Ranges (CCR), producing a NE–SW-oriented horst-and-graben architecture that controlled early sedimentation along the margin (Roca, 2001).

Tectonic activity waned during the Middle Miocene, marking the onset of post-rift subsidence and large-scale sediment progradation sourced from the Iberian hinterland (Escutia and Maldonado, 1992; Roca, 2001). Two major post-rift megasequences dominate the stratigraphic architecture of the Ebro Margin: the Serravallian–Messinian *Castellón Group*, up to ~1 km thick, and the Plio–Quaternary *Ebro Group*, which records sustained shelf and slope progradation and the development of a wide continental shelf extending more than 70 km into the Valencia Trough (Bertoni and Cartwright, 2005; Kertznus and Kneller, 2009).

These two megasequences are separated by the Messinian Erosional Surface (MES), formed during the MSC, when restriction of Atlantic–Mediterranean exchange led to major base-level fall (Hsü et al., 1973; Krijgsman et al., 1999; Garcia-Castellanos et al., 2009), which, along the Ebro Margin, produced deep

fluvial incision into Miocene clinoforms and the development of a prominent Messinian canyon system (Urgeles et al., 2011; Cameselle et al., 2014).

The onshore Ebro Basin is the largest Cenozoic foreland basin of the Iberian Peninsula, bounded by the Pyrenees, Iberian Ranges, and CCR. Following Late Eocene uplift of the Pyrenees, the basin evolved as an endorheic system until its connection to the Mediterranean, the timing of which remains debated. While some models propose pre-Messinian capture during the Serravallian–Tortonian (García-Castellanos et al., 2003), others emphasise a Messinian linkage driven by base-level fall and regressive erosion (Babault et al., 2006; Urgeles et al., 2011).

2.2 The Messinian Salinity Crisis

The MSC represents one of the most profound paleoceanographic events in the history of the Mediterranean Sea, occurring at ca. 6 Ma (Hsü et al., 1973). Progressive restriction of the Atlantic–Mediterranean connection at the Strait of Gibraltar over approximately 650 kyr (Krijgsman et al., 1999) led to a sharp increase in basin salinity and the accumulation of kilometre-scale evaporitic sequences across the deep Mediterranean basins. Early seismic reflection surveys conducted in the 1970s (Ryan, 1978) revealed the presence of up to 2 km of high-velocity, acoustically transparent evaporites, providing the first basin-wide evidence for extreme Messinian drawdown and evaporite deposition.

Despite decades of intensive research aimed at reconstructing the sequence of events during the MSC, fundamental questions regarding its mechanisms, timing, and hydrological consequences remain actively debated (see review in Roveri et al.,

2014a). A widely adopted conceptual framework emerged following the CIESM synthesis (2008), building on earlier two-stage models (Clauzon et al., 1996) and subdividing the MSC into three main stages.

Stage 1 (5.97–5.60 Ma; ~370 kyr) is characterized by progressive restriction of Atlantic inflow, increasing salinity, and the deposition of gypsum predominantly within peripheral basins. Stage 2 (5.60–5.55 Ma; ~50 kyr) marks peak salinity conditions, widespread erosion of continental margins, and massive halite accumulation in deep basins, during which most authors infer the maximum Mediterranean base-level fall (reviewed by Roveri et al., 2014a). Stage 3 (5.55–5.33 Ma; ~220 kyr), commonly referred to as the Lago-Mare phase, records the accumulation of gypsum and/or clastic sediments associated with brackish-water faunal assemblages, reflecting fluctuating base level and partial reconnection (Andreetto et al., 2021).

The MSC terminated abruptly at the onset of the Pliocene during the Zanclean, when the re-establishment of normal marine circulation restored fully marine conditions throughout the Mediterranean basin (Hsü et al., 1973; García-Castellanos et al., 2009).

2.3 The Ebro drainage before and during the MSC

Whereas the current Ebro River drains the Ebro foreland basin (between the Pyrenees and Iberian ranges (Fig. 1), the main Ebro Basin was once endorheic (i.e., self-contained) during the Oligo-Miocene, and formed in response to tectonic shortening (Nichols, 2004). When drainage was restricted to the endorheic basin,

alluvial-lacustrine sediment accumulated only in the foreland from the Late Eocene to the Late-Middle Miocene (Riba et al., 1983; Puigdefàbregas and Souquet, 1986; Perez-Rivarés et al., 2004; Fig. 1). It is argued that the formerly endorheic basin became externally drained through fluvial capture and sediment overfilling, with the Messinian sea-level fall likely exerting only a secondary influence, and the drainage shift of the Ebro Basin toward the Mediterranean occurring between roughly 13.5 and 8.5 Ma (2003 García-Castellanos et al., 2003; Cameselle et al., 2014). In contrast to models proposing a pre-Messinian opening of the basin based on onshore drainage evolution (Nichols, 2004), offshore seismic stratigraphy demonstrates that the most significant phase of incision affecting the margin is strictly confined to the MES, indicating that deep canyon formation postdates Miocene sedimentation and is genetically linked to Messinian base-level change (Urgeles et al., 2011).

Despite the progradation of coastal/deltaic deposits on the Ebro margin (Evans & Arche, 2002), no major Late Messinian fluvial incision is identified onshore. Consequently, the Messinian Ebro valley must have been relatively short and shallow in length and depth, respectively, and regressive erosion was not extensive onshore, unlike other Messinian Mediterranean rivers (e.g., Nile and Rhône rivers; Barber, 1981; Pellen et al., 2019; Do Couto et al., 2024). The main phase of valley incision is most likely constrained to the MSC Stage 2, when Mediterranean base-level fall and subaerial exposure of the margin were maximal (Roveri et al., 2014a; Aloisi et al., 2025). A polyphase evolution of the MES involving a dominant erosional phase followed by reduced fluvial activity under fluctuating base level

213 can be considered according to studies regarding the terminal stage of the MSC
214 (Andreetto et al., 2021, 2022). This framework places the development of the
215 Messinian Ebro canyon system firmly within the MSC, with potential multiple
216 erosional pulses associated with distinct stages of the crisis.

217

218 **2.4 Seismic-stratigraphy**

219 The seismic stratigraphic analysis of the Ebro Margin follows the framework of
220 Urgeles et al. (2011) and identifies the MES as a regionally extensive unconformity
221 separating the pre-Messinian prograding deposits of Unit B (*Castellon Group,* see
222 section 2.1) from the post-Messinian deposits of Unit D (*Ebro Group,* see section
223 2.1) (Fig. 2). Unit B is truncated at its top by the MES, which evolves basinward
224 into a paraconformity and is recognised in seismic data either as a sharp reflector
225 termination or locally as a continuous high-amplitude negative reflection,
226 particularly along major valley floors (Fig. 2). Borehole calibration confirms the
227 Messinian age of this erosional surface (Lanaja et al., 1987; Urgeles et al., 2011).
228 Directly above the MES, a thin unit (Unit C; generally <100 ms two-way travel
229 time) onlaps the deepest incisions and distal portions of the erosional relief,
230 displaying stratified, low-amplitude reflections in proximal settings and partially
231 stratified to chaotic facies basinward, comparable to Messinian detrital deposits
232 described on other Mediterranean margins (Lofi et al., 2005; Bache et al., 2009).
233 The lateral pinch-out of Unit C coincides with an increase in slope gradient,
234 suggesting deposition near a transient Messinian base level. Given its close spatial

and genetic association with the MES, Unit C, together with the underlying erosional surface (Fig. 2), constitutes the primary focus of this study.

2.5 Geomorphology and timing of the MES in the Ebro Basin

The MES is found between ~1.25 and 2.8 s two-way travel time (approximately 1.4–3.6 km depth, Urgeles et al., 2011) and forms a laterally continuous but morphologically complex surface roughly parallel to the present-day coastline (Fig. 2A). Seismic geomorphological analyses made by Urgeles et al. (2011) reveal a stepped longitudinal profile organised into three major domains from proximal to distal settings (Fig. 2B): a rugged flat–steep domain (Region I), a relatively smooth low-relief domain (Region II), and a basinward-steepening distal domain (Region III), comparable to Messinian erosional landscapes described along other Mediterranean margins, including the Nile Delta, the Gulf of Lions, and the Levant margin (Barber, 1981; Bertoni and Cartwright, 2006; Lofi et al., 2005; Bache et al., 2009).

Region I displays high-relief erosional topography and a dense dendritic drainage network in which low-order tributaries coalesce into high-order, flat-floored valleys, with local relief exceeding 600 m (Urgeles et al., 2011). Although minor post-Messinian extensional tectonics locally affect the relief, particularly in the southwestern part of the survey, MES morphology is dominantly erosional, and comparable rugged landscapes extend beyond the study area in adjacent seismic datasets (Stampfli and Höcker, 1989; Frey-Martínez et al., 2004; Bertoni and Cartwright, 2005). Basinward, Region II corresponds to a gently southeast-dipping,

low-relief surface where incision is restricted to higher-order channels and relief generally remains below ~200 m, separated from Region I by an abrupt but non-tectonic boundary (Urgeles et al., 2011). Region III occupies the outer margin near the present shelf break and is overlain by partially stratified to chaotic deposits (Fig. 2), where assessment of MES relief is locally limited by time–depth conversion uncertainties. Further down, channel disappearance and the pinch-out of Unit C mark a relatively stable base level, indicating short-lived exposure of intermediate domains and a dominantly subaerial, polyphase erosional history linked to Messinian base-level fall (Fig. 2B). It should also be noted that, basinward of Region III and along the downstream continuation of the mapped channels (Fig. 2B), mass-transport deposits (MTDs) and chaotic sediments have been identified (e.g., del Olmo, 2011; Cameselle and Urgeles, 2017).

While the Ebro channel systems have been clearly recognised and mapped (Fig. 2B), the processes responsible for their formation, the hydrological conditions under which they developed, and their relationship to Messinian base-level change remain poorly constrained, highlighting a critical knowledge gap that this study aims to address.

3. Data and Methods

3.1. Seismic dataset and processing

This study is based on a high-resolution 3D seismic reflection survey covering ~2700 km² of the Ebro Margin. The seismic data were acquired by British Gas BV in 2002 and processed to near–zero phase using a single-pass 3D pre-stack time

migration. The resulting seismic cube has an original horizontal sampling of 12.5 × 12.5 m and a vertical sampling interval of 4 ms two-way travel time (TWT). For this study, the dataset was subsampled to a grid spacing of 25 × 25 m to optimise computational efficiency while preserving geomorphic features.

The data are displayed in SEG (Society of Exploration Geoscientists) normal polarity, such that an increase in acoustic impedance corresponds to a positive amplitude. The stratigraphic interval analysed spans approximately the upper 2.5–3.5 s two-way travel time (TWT). Dominant seismic frequencies near the Messinian Unconformity (MES) are ~30 Hz, yielding an average vertical resolution of ~35 m, with seismic P-wave velocities immediately above the MES reaching ~4250 m s^{-1}. These values are estimated directly from the seismic data and from interval velocities derived from P-wave velocity logs in the FORNAX-1 well used and analysed in Urgeles et al. (2011, their *METHOD* section).

3.2. Well control and stratigraphic calibration

Seismic interpretation has been calibrated using wireline logs from the FORNAX-1 well in Urgeles et al. (2011), including P-wave velocity, S-wave velocity, and gamma-ray logs. Additional stratigraphic constraints are derived from published industry well reports on the Ebro Margin (Lanaja et al., 1987) and correlations with regional seismic interpretations (Frey-Martínez et al., 2004; Bertoni and Cartwright, 2005). A synthetic seismogram was also generated in Urgeles et al. (2011; their Figure 4). A representative wavelet was extracted using frequency-

303 matching techniques from seismic traces within a 500 m radius around the well.
304 This synthetic tie ensures consistent placement of stratigraphic horizons in time.
305
306 **3.3 Identification and mapping of the Messinian Erosional Surface**
307 The MES and associated fluvial features were mapped on zero-phase seismic data
308 in two-way travel time. The MES horizon used here is modified from the regional
309 interpretation of Urgeles et al. (2011), who demonstrated its Messinian age based
310 on borehole calibration and stratigraphic relationships. The MES is identified by
311 truncation of Miocene clinoforms, reflector terminations, and, locally, by a
312 continuous high-amplitude reflector at the base of major valleys.
313 Mapping and horizon propagation were performed using the SISMAGE-CIG™
314 interpretation platform. Channel bases and associated deposits were semi-
315 automatically propagated and manually quality-controlled to ensure consistency
316 across the seismic volume. Seismic sections are shown in two-way-time TWT.
317 *Detailed descriptions of the seismic-derived paleotopographic analyses of the MES,*
318 *including drainage extraction, geomorphic metrics, and paleodischarge*
319 *calculations using Manning's equation and an independent width–discharge*
320 *relationship (Attal et al., 2008), are provided in the Supplementary Material.*
321

322 **4. Results**

323 **4.1 The Messinian Ebro River**
324 Re-investigation of the MES and further, more accurate mapping reveals the
325 presence of vast, detailed channelised features, aggrading above the Messinian

326 paleo-landscape (Fig. 3). In region I, a major NW-SE, 2km wide valley, with ~1300
327 m of relief is visible over a map of the MES, with two major valleys (N-S and E-
328 W) serving as tributaries of the main valley (Fig. 3A-C). Downstream, the valley
329 widens to 3.5km in region II and up to ~4km in region III (Fig. 3).

330 At the stratigraphic base of the system, the widest channel (Channel "C0") (width
331 from 500m upstream up to ~4000m downstream), is characterised by a high
332 amplitude seismic reflector, also clearly visible in map-view, flowing across an
333 entire flat-based valley (Fig. 3A-C), with infilled morphology, overbank deposits
334 and associated splays (Fig 3A-C). Its thalweg is mainly straight (sinuosity: 1.1) over
335 the studied area. Further downstream, narrower channelised systems (C1 to C4)
336 crosscut some C0 paleo deposits (Fig. 3). C1, the longest and most laterally
337 continuous channel system (Fig. 3A), has numerous meanders (mean sinuosity: 1.4
338 to 1.7) along its path (Fig. 3). Although C0 and C1 share a common upstream
339 thalweg (Fig. 3A), C1 remains confined throughout its path toward the deep basin
340 within the wide valley of C0. C1 then narrows relative to C0, with widths reaching
341 500–650 m in its deepest section. C1 is fed downstream by several tributaries (C2–
342 C4) that converge into its course, as seen on the amplitude map of Fig. 3A-B.
343 Seismic cross-sections show that C1 is consistently incising the basal surface of the
344 earlier, wider channel C0 (as seen in 3D visualisation, Fig. 3C), while tributaries
345 C2–C4 terminate within the stratigraphic level of C1 and locally truncate C0
346 deposits (Fig. 3). In plan view, C2–C4 align with the meandering thalweg of C1
347 and display comparable sinuosity values, in contrast to the straighter geometry of
348 C0 (Fig. 3A). In addition, crevasse splays associated with C1 locally crosscut C0

deposits (Fig. 3B), demonstrating active sedimentation linked to C1 after abandonment of C0.

4.2 Discharge estimates and topographic analyses

The map of the MES was analysed to assess the features of the Messinian topography (Fig. 3A). To calculate River discharges, we used two approaches: one based on applying the Manning's equation (Fig. 4B-C, Fig. S2, Table S1), and another based on channel width (Fig. 4B, Fig. S3, Attal et al., 2008). Along cross sections of C0 (Fig. 4A), we calculated a discharge of C0 that reached an average of ~2.4×10^5 m^3/s, indicating an extraordinary outflow regime (Figs. 4A-C) (see *Discussion* below). Fig. 4B reveals that in the downstream part of C0-C1, alluvial terraces are visible. The catchment of the channels C1 to C3 is estimated to be at least 1070 km^2 (Fig. 4A). The longitudinal stream profiles show that the main trunk (C1) has the gentlest profile compared to C2 and C3 (Fig. 4A, 4D). The stream profiles also show knickpoints on channels C2 and C3 (Fig. 4D). Discharge estimates derived from Manning's equation are inherently sensitive to both channel slope and the choice of the roughness coefficient (n), particularly when slopes are measured on seismic-derived paleo-surfaces that may include local noise. To account for these uncertainties, discharge was calculated using conservative slope estimates and a fixed roughness coefficient ($n = 0.05$, Following Garcia-Castellanos et al. 2009), and minimum–maximum discharge ranges were derived based on channel geometry. Despite these uncertainties, discharge estimates obtained from Manning's equation and from width–discharge scaling are of the same order of

372 magnitude and display consistent downstream trends (Fig. 4), including an increase
373 in discharge following the confluence of tributaries C2–C4 into C1.

374 Discharge values estimated from both methods (i.e., Manning formula and the
375 width of C1) yield similar results (Fig. 4) and show an increase in downstream
376 discharge after C2-C4 merged with C1, as expected for fluvial systems. Both
377 methods indicate lower discharge for C1 than for C0, suggesting an initial abrupt
378 outflow from the Ebro endorheic basin, followed by more moderate flow (Fig. 4B)
379 (see *Discussion*).

380 As a complementary analysis, we explored scaling relationships of the drainage
381 network developed on the MES using Hack's and Flint's laws, with the aim of
382 characterising the geometry and degree of adjustment of the fluvial system rather
383 than independently constraining uplift magnitude or base-level change. Application
384 of Hack's law yields an h-exponent of ~0.48 (Fig. 4D), a value well within the broad
385 range reported for natural river systems under relatively homogeneous conditions
386 (approximately 0.4–0.7; Rigon et al., 1996; Hergarten et al., 2016). Scaling
387 relationships derived from Hack's and Flint's laws were explored to characterise
388 the geometry of the drainage network developed on the Messinian Erosional
389 Surface, but not to independently infer uplift magnitude or base-level change.
390 Hack's law analysis yields an h-exponent of ~0.48 (Fig. 4D), a value that lies within
391 the range of ~0.4–0.7 reported for drainage systems evolving under relatively
392 homogeneous conditions (Whipple et al., 2013; Hergarten et al., 2016). A much
393 wider range of h-values, from <0.2 in steep headwater channels to >1 in some
394 alluvial systems, has been documented elsewhere and reflects variations in drainage

maturity, lithology, and relief rather than a single controlling process (Brummer and Montgomery, 2003; Sofia et al., 2015). Given the scatter observed in the length–area relationship and the limited spatial extent of the analysed catchments (Fig. 4E), the estimated h-exponent is therefore to be taken with caution for our diagnostic of base-level change.

Flint's law analysis yields a concavity index θ of ~0.30 and a channel steepness index ks of ~8.2 (Fig. 4E). As noted by Hergarten et al. (2010), a strong positive correlation between surface elevation and channel slope exists in several orogens, implying that apparent concavity indices may increase simply due to systematic variations in elevation and uplift rate along river profiles. Such behaviour is consistent with drainage systems developed in small, recently formed, hard-rock mountain belts such as the Catalan Coastal Ranges, where relatively high slopes persist across scales (Hergarten et al., 2016). Importantly, because both Hack's and Flint's laws assume drainage systems close to equilibrium, their applicability to a transient system affected by rapid incision and short-lived high-discharge events remains limited, and these metrics are therefore used here in a descriptive rather than strictly diagnostic sense.

5. Discussion

5.1 Did C0 represent a (fluvial) valley-scale flow event?

A key assumption underlying the discharge estimates for C0 is that flow occupied a large fraction of the flat-floored valley during incision. An alternative interpretation is that the wide valley resulted from progressive lateral migration or repeated occupation by a narrower channel, subsequently abandoned and terraced prior to incision by C1. Several observations argue against this latter scenario. First, the C0 surface is laterally continuous over several kilometres and displays a remarkably uniform, flat basal morphology, inconsistent with the diachronous widening expected from sustained meandering or lateral erosion by a confined channel (Fig. 3). Second, internal seismic facies within C0 lack evidence for multiple stacked point-bar accretion surfaces or lateral migration packages, and instead show laterally extensive, low-relief geometries compatible with rapid aggradation or abandonment following a high-discharge event (Fig. 3, Figs S6-8, S10). Third, crevasse splays and overbank deposits associated with C0 extend across the full width of the valley (Fig. 3A), indicating flow overtopping channel margins rather than confinement to a narrow thalweg. Finally, the sharp incision of C1 into C0 deposits, together with the preservation of flanking amplitude contrasts, and terrace-like remnants across the valley floor, implies rapid abandonment of a broad depositional surface rather than gradual narrowing through time.

The interpretation of C0 as a valley-scale flow event is consistent with a dominantly subaerial fluvial origin for the drainage system in Region I, as previously proposed by Urgeles et al. (2011). We acknowledge that branching channel patterns alone are

not diagnostic of subaerial conditions, as dendritic networks may also develop in submarine canyon systems (e.g., Moneron and Gvirtzman, 2022). However, in the Ebro Margin, the combination of low-gradient thalwegs, meandering planforms, valley-filling overbank deposits, terrace development, and the absence of neither evaporitic material over the MES, nor headward-sapping geometries anywhere along the observed drainage systems collectively favours erosion dominated by discharge-driven fluvial processes rather than submarine slope-controlled incision. In any case, while base-level lowering does not uniquely require eustatic sea-level fall, the stratigraphic confinement of C0 incision to the MES links this valley-scale flow event to Messinian base-level change, irrespective of whether drawdown was fully subaerial or partly submarine.

5.2 Can climatic conditions alone explain the formation of major MSC rivers?

While it has been argued that the opening of the Ebro Basin started long before the MSC; and most likely facilitated by periods of wetter climatic conditions (Garcia-Castellanos et al., 2003; Urgeles et al., 2011), our results suggest a different story. Although major discharge in rivers can be historically explained by climatic changes (i.e., from arid to wet), this exceptional outflow (~2.4×10^5 m^3/s) is 20 times higher than that of the Ebro River historic floods of 1787 and, which reached a peak discharge of 12.9×10^3 m3/s and $11.5 \cdot 10^3$ m^3/s, Ruiz-Bellet et al., 2017 ; Balasch et al., 2019), respectively. The estimated apparent paleo-discharge of C1 appears to be in the same range or lower than these floods. The estimated value of the C0 discharge is in the range of apparent paleo-discharges observed for sudden

outburst floods such as that in Lake Agassiz (*i.e.,* 100-600·10^3 m^3/s, Tinkler & Pengelly, 1995) but lower than flooding discharge estimated during the MSC on the Gibraltar sill (10^8 m^3 s^{-1}, Garcia-Castellanos et al., 2009) and on the Sicilian sill (47.4 10^6 m^3s^{-1}, Spatola et al., 2020). These comparisons should be viewed cautiously as the contributing drainage areas, stored water volumes, and boundary conditions differ substantially among these systems, and similar discharge magnitudes do not imply directly comparable basin sizes or flood mechanisms.

Despite generally arid conditions in the western Mediterranean, the Messinian Ebro margin experienced comparatively wetter climates and higher mean precipitation (Fauquette et al., 2006), consistent with the observed channel morphology and inferred discharges following the major C0 outflow. Moreover, the absence of chaotic seismic facies, headwall scarps, or amphitheater-shaped heads typical of submarine landslides, together with the presence of laterally continuous reflectors and well-preserved meandering channel geometries, indicates that these features do not result from mass-transport processes but instead reflect a dominantly fluvial origin governed by discharge dynamics rather than slope failure or sapping under extreme climatic conditions.

Taken together, these observations suggest that a catastrophic lake-outburst flood provides the most plausible explanation for such extreme flow within a basin of this size. We therefore infer that the Ebro paleo-lake was fully drained during the Messinian sea-level fall, its outburst explaining the scale and morphology of channel C0.

5.3 Driving mechanisms and chronology of events

This study provides the first documentation of a basin-scale response to the MSC: the complete drainage of an endorheic lake system induced by base-level fall (estimated to be around 1200 to 1500m in the western Mediterranean Sea, as suggested by Clauzon, 1982, Loget et al., 2006, Bache et al., 2009) (Fig. 5A-B). The resulting outflow represents a previously unrecognised mechanism linking Mediterranean drawdown to continental drainage reorganisation. Notably we provide the first evidence of Messinian alluvial terraces, documenting post-outburst fluvial re-incision, potentially contemporaneous with flexural uplift (see Figure S9).

The stacked C0–C1 terrace remnants record up to ~150 m of relative vertical motion across the valley floor (Figs. 2–4), indicating renewed incision following abandonment of the initial high-discharge channel. While this change primarily reflects fluvial re-incision, its magnitude is comparable to the range of post-Messinian flexural rebound predicted for the Ebro margin (Urgeles et al., 2011; Heida et al., 2021). Flexural modeling presented in the Supplementary Material, assuming effective elastic thicknesses of 10–20 km, yields rebound amplitudes of ~80–140 m, suggesting that isostatic adjustment may have contributed to the observed vertical separation between terrace levels. We therefore interpret the terrace offsets as recording a combination of renewed fluvial incision superimposed on longer-wavelength flexural uplift associated with Messinian base-level change, rather than attempting to quantitatively partition incision and uplift components. The spatial relationship between terrace preservation, valley geometry, and predicted flexural response is discussed qualitatively in the Supplementary

Material, where sensitivity tests illustrate the first-order influence of elastic thickness on rebound magnitude (Fig. S9).

Here, our observations collectively indicate that canyon incision along the Ebro margin reached its peak during the lowstand phase of the MSC, when rapid regressive erosion triggered the opening of the Ebro endorheic basin and a short-lived but catastrophic lake outburst flood (Fig. 4C, t_1–t_2). This event excavated the broad, high-discharge channel C0 and initiated deep canyon formation. The subsequent decrease in discharge during continued lowstand conditions and flexural isostatic rebound allowed for renewed incision by narrower, meandering channels (C1–C4; Fig. 4, t_3) and formation of alluvial terraces, consistent with a transition from catastrophic outflow to sustained fluvial reorganisation as base level and hydrological conditions stabilised. The return to normal marine conditions led to progressive burial of the Messinian landscape under Pliocene–Quaternary sediments, preserving its relict fluvial morphology Fig. 4C, t_4).

From a broader perspective, this interpretation also contrasts with earlier models proposing that the Ebro Basin opened well before the Messinian (13-8.5 Ma), through fluvial capture and progressive sediment overfilling, with the Messinian sea-level fall playing only a minor role (Evans and Arche, 2002; García-Castellanos et al., 2003; Cameselle et al., 2014). Our results instead point to a later, MSC-linked drainage event, in which the rapid base-level fall directly triggered basin breaching and catastrophic lake outflow.

6. Conclusions

This study provides integrated seismic, geomorphic, and hydrological evidence that the Messinian Salinity Crisis triggered the complete drainage of a formerly endorheic Ebro Basin through rapid Mediterranean base-level fall. Analysis of the Messinian Erosional Surface reveals a polyphase fluvial evolution along the Ebro Margin, characterised by two fundamentally different incision regimes. An initial phase involved a lowstand-induced regressive erosion that triggered a short-lived, high-magnitude lake-outburst flood that excavated a broad, flat-floored valley (C0) and initiated deep canyon formation. This phase was followed by a second stage of lower-energy, more sustained fluvial incision, during which narrower, meandering channels (C1–C4) reworked the valley floor, producing stepped alluvial terraces. These observations indicate a transition from catastrophic outflow to organised fluvial adjustment as hydrological conditions evolved and base level stabilised during the later stages of the MSC. The scale of the inferred discharge, the valley-wide extent of C0, and the stratigraphic confinement of incision to the MES together support a model in which basin breaching and drainage were directly linked to Messinian drawdown, rather than inherited from earlier Miocene drainage capture.

The preservation of this relict fluvial landscape beneath thick post-Messinian deposits provides an exceptional stratigraphic archive of transient canyon formation and rapid landscape adjustment to extreme base-level change. More broadly, this study illustrates how short-lived, high-magnitude hydrological events can exert a first-order control on continental-scale drainage reorganisation and margin incision during periods of abrupt environmental change.

Declaration of competing interest

The authors declare that they have no known competing financial interests or personal relationships that could have appeared to influence the work reported in this paper.

Acknowledgments

This work was done in the scope of the *Seismic Geomorphology* research project of TotalEnergies SE, which we thank for providing access to seismic data and a SISMAGE license.

References Cited

Aloisi, G., Moneron, J., Guibourdenche, L., Camerlenghi, A., Gavrieli, I., Bardoux, G., Agrinier, P., Ebner, R., and Gvirtzman, Z., 2024, Chlorine isotopes constrain a major drawdown of the Mediterranean Sea during the Mes sinian salinity crisis: Nature Communications, v. 15, 9671, https://doi .org /10 .1038 /s41467-024-53781-6.

Andreetto, F., Aloisi, G., Raad, F., Heida, H., Flecker, R., Agiadi, K., ... & Krijgsman, W., 2021. Freshening of the Mediterranean Salt Giant: controversies and certainties around the terminal (Upper Gypsum and Lago-Mare) phases of the Messinian Salinity Crisis. *Earth-Science Reviews*, *216*, 103577.

Andreetto, F., Flecker, R., Aloisi, G., Mancini, A. M., Guibourdenche, L., de Villiers, S., & Krijgsman, W., 2022. High-amplitude water-level fluctuations at the end of the Mediterranean Messinian Salinity Crisis: Implications for gypsum formation, connectivity and global climate. *Earth and Planetary Science Letters*, *595*, 117767

Attal, M., Tucker, G. E., Whittaker, A. C., Cowie, P. A., and Roberts, G. P., 2008, Modeling fluvial incision and transient landscape evolution: Influence of dynamic channel adjustment, J. Geophys. Res., 113, F03013, doi:10.1029/2007JF000893.

Babault, J., Loget, N., Van Den Driessche, J., Castelltort, S., Bonnet, S. & Davy, P., 2006. Did the Ebro Basin connect to the Mediterranean before the Messinian salinity crisis? Geo morphology, 81, 155^165.

580 Bache, F., Olivet, J.L., Gorini, C., Rabineau, M. ,Baztan, J., Aslanian, D. &
581 Suc, J.-P., 2009. Messinian erosional and salinity crises: view from the Provence
582 basin (Gulf of Lions, Western Mediterranean). Earth and Planetary Science Letters,
583 286,139^157.

584 Bahia, R., Jones, M., Covey-crump, S.J., & Mitchell, N.C., 2019, The
585 application of Hack's law and Flint's law to Mars and its implications for the
586 Noachian climate (LPI contribution No. 2132).

587 Baker, V.R., Milton, D.J., 1974, Erosion by catastrophic floods on Mars and
588 Earth. Icarus 23, 27–41.

589 Balasch J.C., Pino D., Ruiz-Bellet J.L., Tuset J., Barriendos M., Castelltort
590 X., Peña J.C., (2019). The extreme floods in the Ebro River basin since 1600 CE,
591 Science of The Total Environment, v.646, 645-660.

592 Barber, P. M., 1981. Messinian subaerial erosion of the proto-Nile
593 Delta. *Marine Geology*, *44*(3-4), 253-272.

594 Bertoni, C. & Cartwright, J., 2005, 3D seismic analysis of slope-confined
595 canyons from the Plio-Pleistocene of the Ebro Continental Margin (Western
596 Mediterranean). Basin Research, 17,43^62.

597 Bertoni, C., & Cartwright, J. A., 2006. Controls on the basinwide
598 architecture of late Miocene (Messinian) evaporites on the Levant margin (Eastern
599 Mediterranean). *Sedimentary Geology*, *188*, 93-114.

Brummer, C. J., & Montgomery, D. R., 2003. Downstream coarsening in headwater channels. *Water Resources Research*, *39*(10).

Cameselle, A. L., Urgeles, R., De Mol, B., Camerlenghi, A., & Canning, J. C., 2014. Late Miocene sedimentary architecture of the Ebro Continental Margin (Western Mediterranean): implications to the Messinian Salinity Crisis. *International Journal of Earth Sciences*, *103*(2), 423-440.

Cameselle, A. L., & Urgeles, R., 2017. Large-scale margin collapse during Messinian early sea-level drawdown: The SW Valencia trough, NW Mediterranean. *Basin Research*, *29*, 576-595.

Chumakov, I. S., 1973. Pliocene and Pleistocene deposits of the Nile valley in Nubia and upper Egypt, Initial Rep. Deep Sea Drill. Proj., 13, 1242- 1243.

Clauzon, G., 1982, Le canyon messinien du Rhône: Une preuve decisive du desiccated deep-basin model (Hsü , Cita et Ryan, 1973), Bull. Soc. Géol. Fr., 24, 597–610

Clauzon, G., Suc, J. P., Gautier, F., Berger, A., & Loutre, M. F., 1996. Alternate interpretation of the Messinian salinity crisis: controversy resolved?. *Geology*, *24*(4), 363-366.

Do Couto, D., Cushing, E. M., Mocochain, L., Rubino, J. L., Miquelis, F., Hanot, F., ... & Bellier, O., 2024. Messinian canyons morphology of the Rhône and Ardèche rivers (south-east France): new insights from seismic profiles. *BSGF-Earth Sciences Bulletin*, *195*(1), 19.

621 Druckman, Y., Buchbinder, B., Martinotti, G.M., Siman-Tov, R.&
622 Aharon,P., 1995. The buried A¢qCanyon (eastern Mediterranean, Israel), a case
623 study of a Tertiary submarine canyon exposed in Late Messinian times. Mar. Geol.,
624 123, 167^185.

625 Evans, G., Arche, A., 2002, The flux of siliciclastic sediment from the
626 Iberian Peninsula, with particular reference to the Ebro. In: Jones SJ, Frostick LE
627 (eds) Sediment flux to basins: causes, controls and consequences. Geol Soc Spec
628 Publ, London, pp 199–208.

629 Escutia, C., Maldonado, A., 1992. Paleogeographic implications of the
630 Messinian surface in the Valencia trough, northwestern MediterraneanSea. In:
631 Banda, E., Santanach, P. (Eds.), Geology and Geophysics of the Valencia Trough,
632 Western Mediterranean. Tectonophysics, 203, 263–284.

633 Fauquette, S., Suc J-P., Bertini A., et al., 2006, How much did climate force
634 the Messinian salinity crisis? Quantified climatic conditions from pollen records in
635 the Mediterranean region, Palaeogeogr. Palaeoclimatol. Palaeoecol., 238, 281– 301.

636 Frey-Martinez, J., Cartwright, J.A., Burgess, P.M., and Vicente-Bravo, J.,
637 2004. 3D seismic interpretation of the Messinian Unconformity in the Valencia
638 Basin, Spain: 3D Seismic Technology: Application to the Exploration of
639 Sedimentary Basins. (Ed. by R.J. Davies, J.A. Cartwright, S.A. Stewart, M. Lappin
640 & J.R. Underhill). Memoirs of the Geological Society, London, 29, 91-100.

641 Garcia-Castellanos, D., J. Vergés, J.M. Gaspar-Escribano and S.
642 Cloetingh, 2003, Interplay between tectonics, climate and fluvial transport during

643 the Cenozoic evolution of the Ebro Basin (NE Iberia).J. Geophys. Res. 108 (B7),
644 2347. doi:10.1029/2002JB002073.

645 García-Castellanos, D., Estrada, F., Jimenez-Munt, I., Gorini, C.,
646 Fernandez, M., Verges, J., & De Vicente, R., 2009. Catastrophic flood of the
647 Mediterranean after the Messinian salinity crisis. *Nature*, *462*(7274), 778-781.

648 Gargani, J., 2004. Modelling of the erosion in the Rhône valley during the
649 Messinian crisis (France). Quat. Int. 121, 13–22

650 Gargani, J., Rigollet, C., Scarselli, S., 2010, Isostatic response and
651 geomorphological evolution of the Nile valley during the Messinian salinity
652 crisis. Bull. Soc. Geol. Fr., v.181, n.1, p.19-26.

653 Gargani, J., Rigollet, C., 2007. Mediterranean sea-level variations during
654 Messinian Salinity Crisis. Geophys. Res. Lett. 34, L10405.
655 http://dx.doi.org/10.1029/2007GL029885.

656 Guennoc, P., Gorini, C., Mauffret, A., 2000. Geological history of the Gulf
657 of Lions: Oligo-Aquitanian rift and Messinian surface maps. Histoire geologique
658 du golfe du Lion et cartographie du rift oligo-aquitanien et de la surface
659 messinienne Geol. Fr. 3, 67e97.

660 Gueguen, E., Doglioni, C., and Fernandez, M., 1998. On the post-25 Ma
661 geodynamic evolution of the western Mediterranean. Tectonophysics, 298, 259-
662 269.

663 Gupta, S., Collier, JS., Palmer-Felgate, A., Potter. G., et al., 2007,
664 Catastrophic flooding origin of shelf valley systems in the English Channel, Nature,
665 Vol: 448, Pages: 342-U5

666 Gvirtzman, Z., Heida, H., Garcia-Castellanos, D., Bar, O., Zucker, E., and
667 Enzel, Y., 2022, Limited Mediterranean sea-level drop during the Messinian
668 salinity crisis in ferred from the buried Nile canyon: Communications Earth &
669 Environment, v. 3, no. 1, https://doi .org /10 .1038 /s43247-022-00540-4.

670 Haq, B., Gorini, C., Baur, J., Moneron, J., and Rubino, J. L., 2020, Deep
671 Mediterranean's Messinian evaporite giant: How much salt?. Global and Planetary
672 Change, 184, 103052. doi: https://doi.org/10.1016/j.gloplacha.2019.103052

673 Heida, H., Raad, F., Garcia-Castellanos, D., Jiménez-Munt, I., Maillard, A.,
674 & Lofi, J., 2022. Flexural-isostatic reconstruction of the Western Mediterranean
675 during the Messinian Salinity Crisis: Implications for water level and basin
676 connectivity. *Basin Research*, *34*(1), 50-80.

677 Hergarten, S., Wagner, T., & Stüwe, K. (2010). Age and prematurity of the
678 Alps derived from topography. *Earth and Planetary Science Letters*, *297*(3-4), 453-
679 460.

680 Hergarten, S., Robl, J., & Stüwe, K., 2016. Tectonic geomorphology at
681 small catchment sizes–extensions of the stream-power approach and the χ
682 method. *Earth Surface Dynamics*, *4*(1), 1-9.

683 Hsü, K. J., Cita, M. B., and Ryan, W. B. F., (1973), The origin of the
684 Mediterranean evaporites, in Kaneps, A. G., ed., Initial reports of the deep sea

685 drilling project, Volume 13: Washington, D. C., U. S. Government Printing Office,
686 p. 1203-1231.

687 Kertznus,V. & Kneller, B., 2009. Clinoform quantification for assessing the
688 effects of external forcing on continental margin development. Basin Research,
689 21,738^758.

690 Krijgsman, W., Hilgen, F. J., Raffi, I., Sierro, F. J. & Wilson, D. S., 1999,
691 Chronology, causes and progression of the Messinian salinity crisis. Nature 400,
692 652–655.

693 Lanaja, J. M., 1987. *Contribución de la exploración petrolífera al*
694 *conocimiento de la geología de España*. IGME.

695 Leverington, D. W., 2011. A volcanic origin for the outflow channels of
696 Mars: Key evidence and major implications. *Geomorphology*, *132*(3-4), 51-75.

697 Lofi, J., Gorini, C., Berné, S., Clauzon, G., Dos Reis, A. T., Ryan, W. B., &
698 Steckler, M. S., 2005. Erosional processes and paleo-environmental changes in the
699 Western Gulf of Lions (SW France) during the Messinian Salinity Crisis. *Marine*
700 *Geology*, *217*(1-2), 1-30.

701 Lofi, J., Sage, F., D´everch`ere, J., Loncke, L., Maillard, A., Gaullier, V.,
702 Thinon, I., Gillet, H., Guennoc, P., Gorini, C., 2011. Refining our knowledge of the
703 Messinian salinity crisis records in the offshore domain through multi-site seismic
704 analysis. Bull. Soc. G´eol. Fr. 182 (2), 163–180.

705 Loget, N., Driessche, J. V. D., & Davy, P., 2005. How did the Messinian
706 salinity crisis end?. *Terra Nova*, *17*(5), 414-419.

Madof, A.S., Bertoni, C., and Lofi, J., 2019, Discovery of vast fluvial deposits provides evidence for drawdown during the late Miocene Messinian salinity crisis: Geology, v. 47, p. 171–174, https://doi .org /10 .1130 /G45873 .1.

Moneron, J., and Gvirtzman, Z., 2022, Late Messinian submarine channel systems in the Levant Basin: Challenging the desiccation scenario: Geology, v. 50, p. 1366–1371, https://doi .org /10 .1130 /G50583 .1.

Moneron, J., Gvirtzman, Z., Karcz, Z., and Sagy, Y., 2024, Discovery of the Messinian Eratosthenes Canyon in the deep Levant Basin: Global and Planetary Change, v. 232, https://doi .org /10 .1016 /j .gloplacha .2023 .104318.

Moneron, J., Gvirtzman, Z., Karcz, Z., Shitrit, O., Sagy, Y., and Aharonov, E., 2025, Exploring the relationship between sedimentary transport systems and basin dy namics: A case study from the Levant Basin (Eastern Mediterranean Sea) before, during, and after the Mes sinian: Geological Society of America Bulletin, v. 137, p. 1423–136, https://doi .org /10 .1130 /B37589 .1.

Nichols, G., 2004, Sedimentation and base level in an endorheic basin : the early Miocene of the Ebro Basin , Spain.

del Olmo, W. M. (2011). El Messiniense en el Golfo de Valencia y el Mar de Alborán: implicaciones paleogeográficas y paleoceanográficas. *Revista de la Sociedad Geológica de España*, *24*(3), 237-257.

Olivet, J.L., 1996. La cinématique de la plaque Ibérique. Bulletin des Centres de Recherches Exploration Production Elf-Aquitaine, 20, 131-195.

728 Pellen, R., Aslanian, D., Rabineau, M., Suc, J. P., Gorini, C., Leroux, E., ...
729 and Rubino, J. L. , 2019, The Messinian Ebro River incision. Global and Planetary
730 Change, 181, 102988. doi: https://doi.org/10.1016/j.gloplacha.2019.102988

731 Pérez-Rivarés, F.J., Garcés, M., Arenas, C., and Pardo, G., 2004,
732 Magnetostratigraphy of the Miocene continental deposits of the Montes de Castejón
733 (central Ebro basin, Spain): Geochronological and paleoenvironmental
734 implications: Geologica Acta, v. 2, p. 221–234.

735 Puigdefàbregas, C., & Souquet, P., 1986. Tecto-sedimentary cycles and
736 depositional sequences of the Mesozoic and Tertiary from the
737 Pyrenees. *Tectonophysics*, *129*(1-4), 173-203.

738 Riba, O., Reguant, S., and Villena, J., 1983, Ensayo de síntesis estratigráfica
739 y evolutiva de la cuenca terciaria del Ebro, in Comba, J., ed., Libro Jubilar J. M.
740 Ríos, Geología de España, Volume 2: Madrid (Spain), Instituto Geológico y Minero
741 de España, p. 131-159.

742 Rigon, R., I. Rodriguez-Iturbe, A. Maritan, A. Giacometti, D. G. Tarboton,
743 and A. Rinaldo, 1996. On Hack's Law, Water Resour. Res., 32(11), 3367–3374,
744 doi:10.1029/96WR02397.

745 Roca, E., 2001. The Northwest Mediterranean Basin (Valencia Trough,
746 Gulf of Lion and Liguro-Provençal basins): structure and geodynamic evolution.
747 Peri-Tethyan Rift/Wrench Basins and Passive margins, 186 (Ed. by P.A. Ziegler,
748 W. Cavazza, A.H.F. Robertson & S. Crasquin-Soleau), pp. 671-706. Peri-Tethys
749 Memoir 6, Mémoires du Museum National d'Histoire Naturelle, Paris.

Roveri, M., Flecker, R., Krijgsman, W., Lofi, J., Lugli, S., Manzi, V., Sierro, F.J., Bertini, A., Camerlenghi, A., De Lange, G., Govers, R., Hilgen, F.J., Hubscher, C., Meijer, P.T., Stoica, M., 2014a. The Messinian salinity crisis: past and future of a great challenge for marine sciences. Mar. Geol. 352, 25–58.

Roveri, M., Manzi, V., Bergamasco, A., Falcieri, F., Gennari, R., Lugli, S., 2014b. Dense shelf water cascading and Messinian canyons: a new scenario for the Mediterranean salinity crisis. Am. Aust. J. Foren. Sci. 314, 751–784.

Roveri, M., Lugli, S., & Manzi, V., 2025. The desiccation and catastrophic refilling of the Mediterranean: 50 years of facts, hypotheses, and myths around the Messinian salinity crisis. *Annual Review of Marine Science*, *17*(1), 485-509.

Ruiz-Bellet, J.L., Castelltort, X., Balasch, J.C., and Tuset, J., 2017, Uncertainty of the peak flow reconstruction of the 1907 flood in the Ebro River in Xerta (NE Iberian Peninsula). Journal of Hydrology, 545, 339-354.

Ryan W.B.F., 1976. Quantitative evaluation of the depth of the western Mediterranean before, during and after the Late Miocene salinity crisis. Sedimentology, v.23, n.6, p. 791-813.

Sofia, G., Tarolli, P., Cazorzi, F., & Dalla Fontana, G. (2015). Downstream hydraulic geometry relationships: Gathering reference reach-scale width values from LiDAR. *Geomorphology*, *250*, 236-248.

Spatola D., del Moral-Erencia J.D., Micallef A., Camerlenghi A., Garcia-Castellanos D., Gupta S., Bohorquez P., Gutscher M.-A., Bertoni C., 2020. A single-stage megaflood at the termination of the Messinian salinity crisis:

772 Geophysical and modelling evidence from the eastern Mediterranean Basin. Marine
773 Geology, v.430, 106337.

774 Stampfli, G. M., & Höcker, C. F. W., 1989. Messinian paleorelief from a
775 3D seismic survey in the Tarraco concession area (Spanish Mediterranean
776 Sea). *Geologie en Mijnbouw*, *68*(2), 201-210.

777 Tinkler, K.J., Pengelly ,J.W.J., 1995. Great Lakes response to catastrophic
778 inflows from Lake Agassiz: some simulations of a hydraulic geometry for chained
779 lake systems. Journal of Paleolimnology, Volume 13, Issue 3, pp 251–266

780 Urgeles, R., Camerlenghi, A., García-Castellanos, D., De Mol, B., Garcés,
781 M., Vergés, J., Haslam I., Hardman, M., 2010. New constraints on the Messinian
782 sealevel drawdown from 3D seismic data of the Ebro Margin, Iberian Peninsula,
783 and implications for the evolution of the Ebro Basin. Basin Res. , doi:
784 https:/doi/org/10.1111/j.1365-2117.2010.00477.x

785 Warner, N, Gupta, S, Muller, J-P, Kim, J-R, Lin, S-Y , 2009, A refined
786 chronology of catastrophic outflow events in Ares Vallis, Mars, Earth and Planetary
787 Science Letters, Vol: 288, Pages: 58-69

788 Whipple, K., Dibiase, R. A., & Crosby, B. T., 2013. Bedrock rivers.
789 In *Fluvial geomorphology* (pp. 550-573). Elsevier Inc..

790
791

792 **Figure Captions**

793

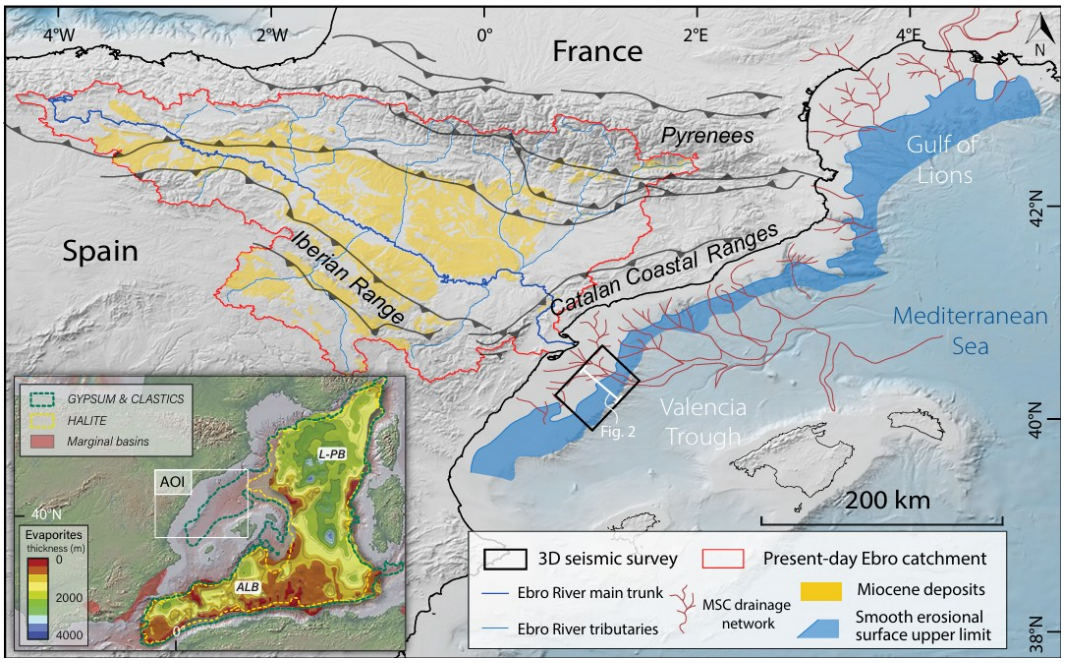

Fig. 1. A. Map showing study area on the Ebro margin, western Mediterranean Sea, offshore NE Spain. Black polygon outlines the extent of the 3D seismic dataset used in this study. Messinian river incision (in dark red, from Pellen et al., 2019) affected all Mediterranean margins, including the Valencia Trough and Gulf of lions. Inset of A is from Haq et al., 2020. AOI-Area of interest, L-PB--Liguro-Provençal Basin ALB—Algero-Balearic Basin.

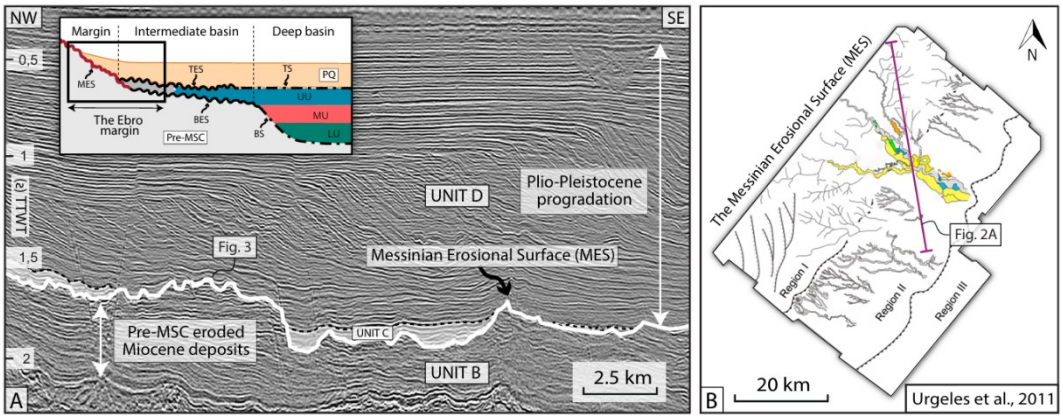

803 **Fig. 2** Typical cross section showing the MES and prograding Plio-Quaternary
804 sediments. Inset of B is modified after Lofi et al., 2005, 2011. More regional
805 seismic cross sections are provided in the Supp. Mat.[1] (Fig. S4). Units B-D from
806 Urgeles et al., 2011.
807

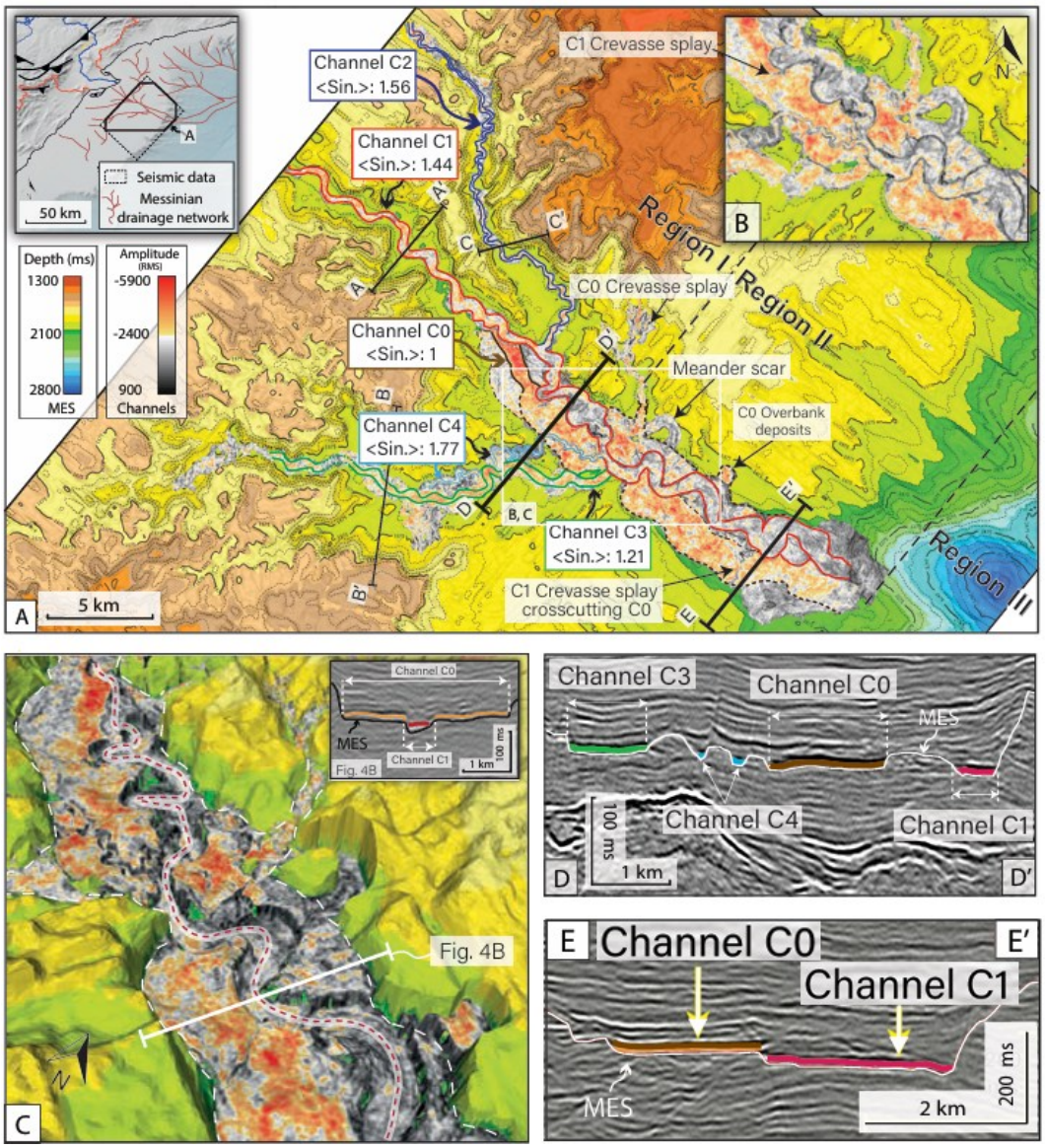

808

809 **Fig. 3. A-B** MES depth map and morphological features in the Ebro valley during
810 the MSC: C0 represents the outflow channel and C1-C4, the meandering channel

observed with 3D seismic data. Seismic sections indicated on the map are shown in Fig. S5, and more 3D visualisations are shown in Fig. S6-8. **C**. 3D view of the main channel C0 being crosscut by the C1 meandering channel. **D-D', E-E'**. Seismic sections illustrating the vertical and lateral arrangement of channels C0-C4. See Fig. S10 for uninterpreted version of A. Grid resolution is 12.5m.

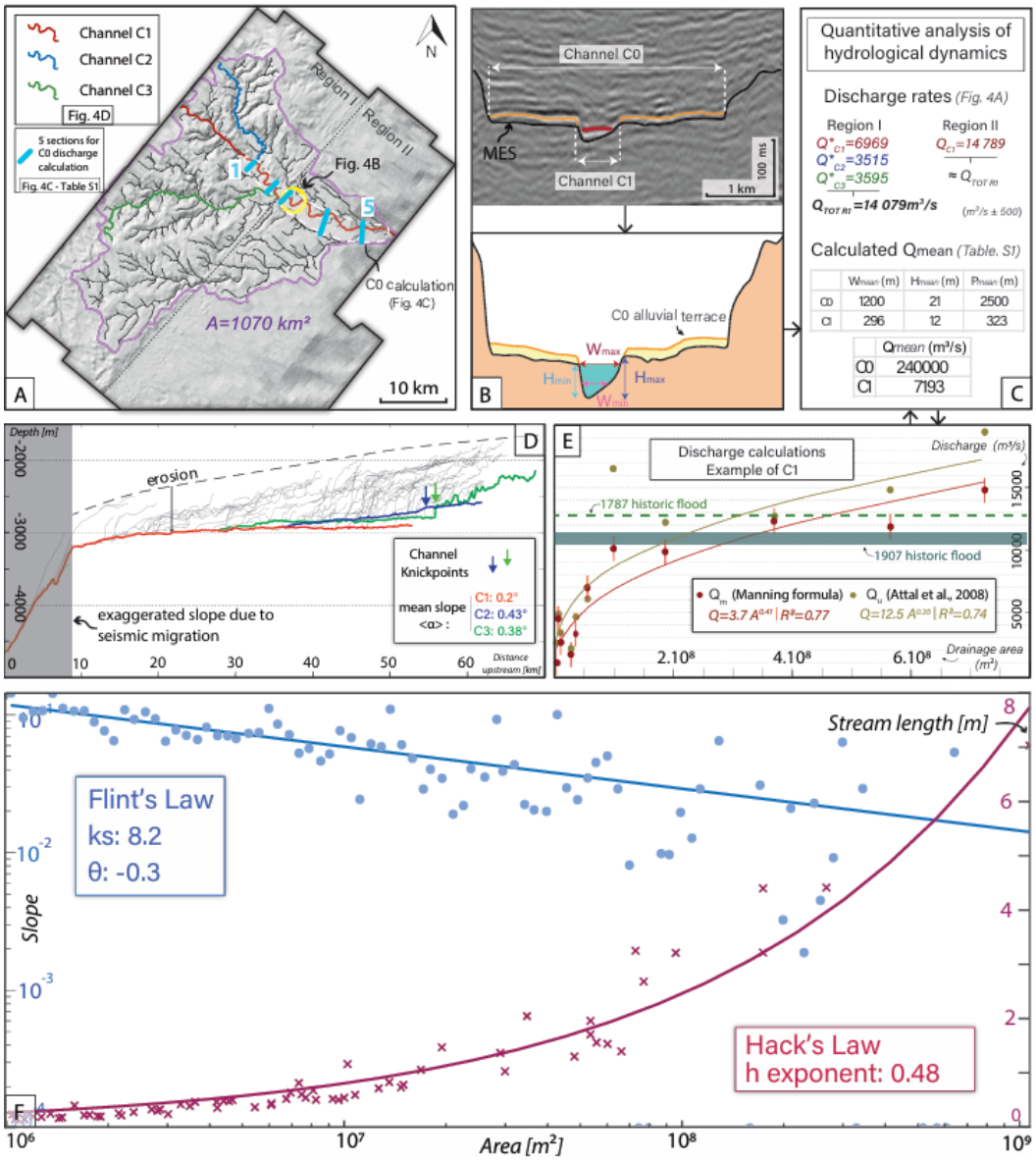

Fig. 4. A. Drainage map extracted from the Messinian Erosional Surface (MES) showing the main channel network (C1–C3) and its ~1070 km² catchment. **B**. Cross-section showing channel C1 incising the earlier high-discharge channel C0. **C**. Quantitative approach for discharge estimation using Manning's equation. The area where calculations were made for C0 is shown in Fig. 4A. **D**. Longitudinal stream profiles highlighting knickpoints in C2–C3. **E.** Discharge estimates for C1 derived from Manning's law and width–area scaling. **F**. Stream length–area and slope–area relationships fitted to Hack's and Flint's laws. Note the significant data scatter and sensitivity to outliers, which limit the precision and interpretability of fitted parameters.

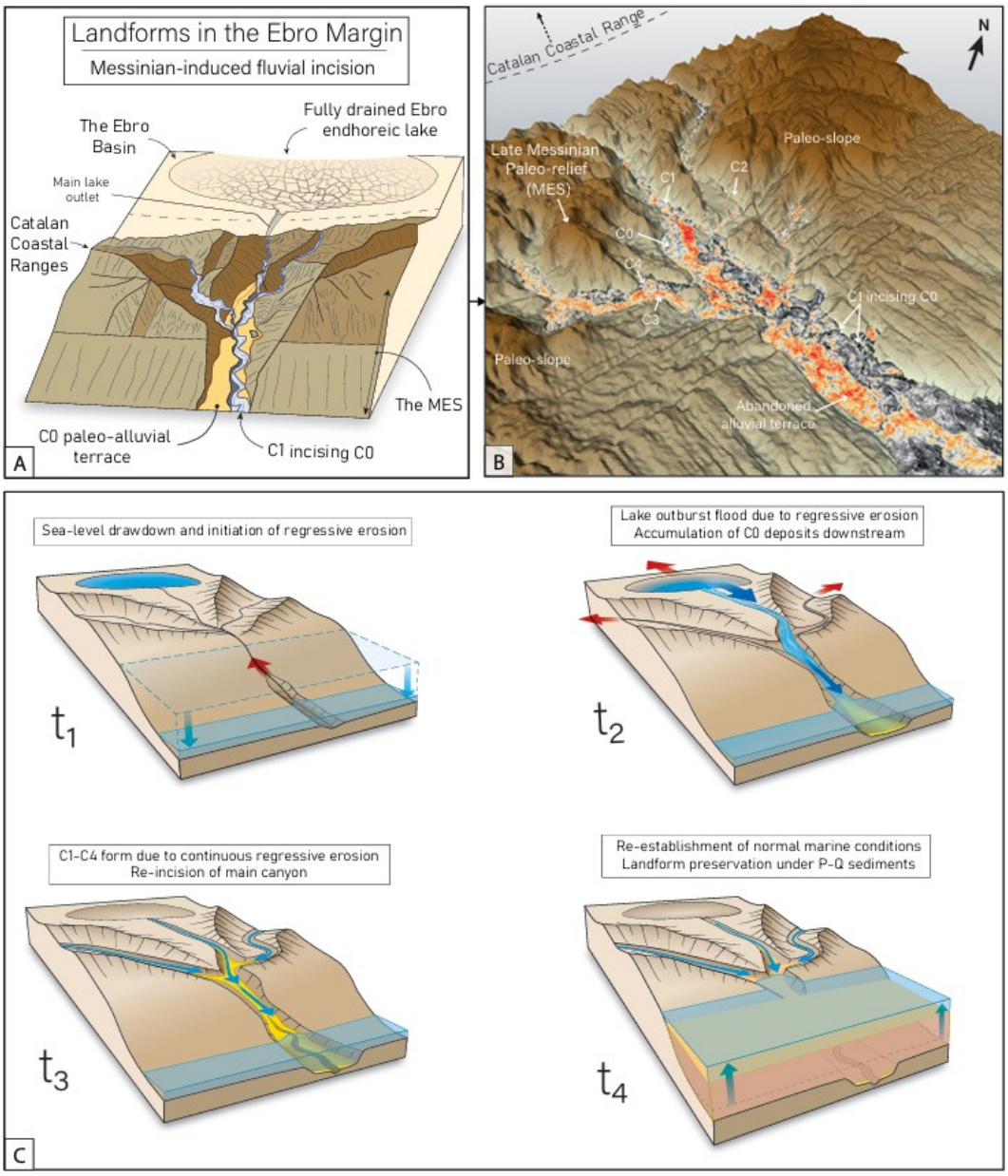

829

830 **Fig. 5. A–B** 3D geomorphic framework showing the Messinian Erosional Surface
831 (MES) paleo-relief, and channel organisation (C0–C4). **C** Four-stage model
832 illustrating the transition from sea-level drawdown and regressive erosion (t_1), to
833 catastrophic lake outburst, canyon formation and accumulation of C0 deposits (t_2),
834 renewed incision by meandering channels C1–C4 under lowstand conditions (t_3),
835 and final burial during Pliocene–Quaternary (P-Q) sedimentation (t_4).